Dynamical numerical model for nematic order reconstruction

G. Lombardo,* H. Ayeb, and R. Barberi
CNR-INFM LiCryL, CEMIF-Center of Excellence for Innovative and Functional Materials, Physics Department, University of Calabria, 87036 Rende, Italy

(Received 4 November 2007; revised manuscript received 26 March 2008; published 29 May 2008)

In highly frustrated calamitic nematic liquid crystals, a strong elastic distortion can be confined on a few nanometers. The classical elastic theory fails to describe such systems and a more complete description based on the tensor order parameter **Q** is required. A finite element method is used to implement the **Q** dynamics by a variational principle and it is shown that a uniaxial nematic configuration can evolve passing through transient biaxial states. This solution, which connects two competing uniaxial nematic textures, is known as "nematic order reconstruction."

DOI: 10.1103/PhysRevE.77.051708 PACS number(s): 64.70.M−, 61.30.Gd

I. INTRODUCTION

Common nematic liquid crystals used, for instance, for electro-optical applications, are aggregates of calamitic molecules without any positional order and whose long axes are in average aligned along a common direction [1]. The most known classical elastic model [2–4] describes a nematic by means of two parameters: The director $\boldsymbol{n}$, a unit vector pointing along the local average molecular orientation, and the scalar order parameter S, which indicates the amount of orientational order. Most phenomena occurring in the nematic phase fit well within this classical description, but, when the elastic distortion occurs over a length scale comparable with the nematic coherence length ξ [1], the molecular order may be significantly altered, and a more complete phenomenological description, using the tensor order parameter **Q**, is required [5]. The eigenvectors $\boldsymbol{e}_1$, $\boldsymbol{e}_2$, and $\boldsymbol{e}_3$ of **Q** are the directions of the preferred molecular orientations and the associated eigenvalues λ_1, λ_2, and λ_3 represent the degree of order along each corresponding direction. Calamitic nematic materials can present three different phases (isotropic, uniaxial, biaxial) which can be distinguishable by considering λ_1, λ_2, and λ_3. In the isotropic phase the calamitic molecules are completely disordered, without any positional and orientational order, and all the three eigenvalues vanish. In this phase, the optical behavior of the material is the same as an ordinary isotropic fluid. The uniaxial nematic phase presents a unique optical axis, described by the eigenvector $\boldsymbol{e}_i \equiv \boldsymbol{n}$ associated to the maximum eigenvalue $\lambda_{\max}$, which gives the scalar order parameter $S=(3/2)\lambda_{\max}$. In the biaxial nematic phase, all the eigenvalues are different and the Fresnel ellipsoid has two optical axes [1].

The **Q** tensor description predicts biaxial domains inside a calamitic nematic phase, as found, for instance, by Sluckin, who demonstrated that, around the core of a defect, the uniaxial nematic order is replaced by a biaxial ring, which connects two orthogonal uniaxial states [6]. Another example is given by Palffy-Muhoray, who predicted that, in a hybrid nematic cell, below a critical distance, the free energy of the system is minimized by a biaxial solution, which connects the two orthogonal uniaxial states promoted by the surfaces [7]. Indeed two uniaxial nematic orthogonal states can be connected by the eigenvector rotation of **Q**, keeping the eigenvalues constant, or by eigenvalues exchange, letting one eigenvalue of **Q** grow at the expense of another one [8]. In the latter case the two uniaxial states are connected through a biaxial state. The biaxial order decays in space with a typical biaxial coherence length ξ_b [9].

Recently, the eigenvalues exchange model has been used to describe experimental results in two relevant cases: Nanoconfined nematic samples in the presence of hybrid anchoring conditions [10,11] and thin π cells submitted to a strong electric field [8,12–14]. First calculations have been carried out by using a numerical approach based on a finite difference method on uniform grid points [8]. However, being the biaxial behavior characterized by two characteristic lengths, the biaxial coherence length ξ_b and the thickness of the cell d, which can easily differ by two orders of magnitude, more sophisticated computational methods are suitable.

In this paper the **Q** tensor model is implemented by using a finite element method (FEM) with an adaptive mesh. The time-dependent **Q** tensor governing equations are derived by balancing the dissipative function and the free energy variations. They are solved by discretizing them in time via an explicit Euler method. The tensor order parameter **Q** is solved by the Galerkin's method [15,16], while the potential profile is updated by the Ritz's method [15,16]. Lagrange quadratic basis functions are employed to interpolate the tensor order parameter and the electric potential over the space. With respect to the previous **Q** tensor description [8], the new model has been improved by adding a third-order term into the elastic density energy, to remove the degeneracy between splay and bend textures and to take into account the temperature dependence of the elastic constants. Moreover, weak and strong anchoring strength conditions are modeled as well.

It is worth to mention that, even though theory based on the continuum model are supposed to work only when the distortion characteristic length is much larger than the molecular size, the **Q** tensor model works well also down to a few nanometers [17–19]. Moreover, very recently, it has been demonstrated that complex molecular dynamical simulations of a nanoconfined nematic twist cell predict similar

*lombardo@fis.unical.it

results of that obtained by the continuum **Q** tensor theory [20].

The paper has the following structure: In Sec. II we introduce the full **Q** tensor model used to describe the dynamical behavior of a nematic phase; in Sec. III we present the main numerical results describing recent experimental evidences on biaxial domains inside frustrated calamitic liquid crystal systems. We also extend results of a very recent semianalytical study on nematic defects subjected to an electric field, including their dynamical behavior. The last section contains our conclusions. Some technical details about the used FEM technique are described in the Appendix.

II. MODEL

A liquid crystal material tends to assume a ground state that minimizes its free energy, which involves its thermodynamical equilibrium state, surface and bulk distortions, and any coupling with external fields. The free energy minimization requires the determination of minimizer's (or more generally of stationary points) of nonlinear functionals of the state variable. As previously stated, two main theories are widely used in nematostatic: The Frank elastic theory, which considers the director as the main state variable, and the Landau–de Gennes approach based on a tensor field description. The Frank theory has generally received more analytical and computational attention. As the director is represented by a unitary vector $\boldsymbol{n}$, the nematic distortions are always represented as spatial director rotations, usually at constant S. This implies that topological defects appear as mathematical singularities and biaxial domains in a calamitic nematic phase are never allowed. Moreover, from a numerical point of view, highly distorted configurations, in which the angle between two neighboring directors may become larger than $\pi/2$, determine technical difficulties for a proper description of the distortion energy [21].

To generalize the Frank continuum model, de Gennes proposed a Ginzburg-Landau expansion for the free energy $\mathcal{F}$ of the liquid crystal close to the nematic-isotropic phase transition temperature. The expansion involves the order parameter **Q** and its spatial derivatives. Nematic distortions are now described by tensor order gradients and biaxial nematic configurations are allowed. In addition, the dynamics of the tensor order parameter is also a crucial issue for the liquid crystal behavior. Therefore, in the following, we first present a general approach based on the **Q** tensor formalism and then we apply this model to quantitatively describe two relevant scientific problems: The bulk and the surface nematic order reconstruction induced by an electric field.

A. Tensor order parameter

Biaxial configurations of calamitic nematics can be described by a symmetric traceless tensor of rank two, **Q**, which can be expressed as

$$\mathbf{Q} = S_1\left(\boldsymbol{n}\otimes\boldsymbol{n} - \frac{1}{3}\mathbf{I}\right) + S_2\left(\boldsymbol{m}\otimes\boldsymbol{m} - \frac{1}{3}\mathbf{I}\right), \tag{1}$$

where $\boldsymbol{n}$, $\boldsymbol{m}$, and $\boldsymbol{n}\times\boldsymbol{m}$ are the eigenvectors of **Q** and the corresponding eigenvalues are $(2S_1-S_2)/3$, $(2S_2-S_1)/3$, and $-(S_1+S_2)/3$, respectively [22]. In the case of uniaxial order, two of the eigenvalues are equal, so either $S_1=0$ or $S_2=0$ or $S_1=S_2$, and the largest eigenvalue is $2S/3$, where S is S_1 or S_2. In the biaxial states, the three eigenvalues are all different and the maximum biaxiality arises when one eigenvalue is zero. In the isotropic state all three eigenvalues vanish.

Nematic configurations are fully defined by five degrees of freedom: Namely, three Euler angles, θ, ϕ, ψ, that define the orientation of the two orthogonal vectors, $\boldsymbol{n}$ and $\boldsymbol{m}$, and the two scalar order parameters, S_1 and S_2. However, when the zenithal angle is $\theta=\pi/2$, the azimuthal angle ϕ is undefined and the solution is not unique [21].

To avoid difficulties due to the multivaluedness of the Euler angles, we restate the problem in terms of five independent components of **Q**,

$$\mathbf{Q} = \begin{pmatrix} q_1 & q_2 & q_3 \\ q_2 & q_4 & q_5 \\ q_3 & q_5 & -q_1-q_4 \end{pmatrix} \tag{2}$$

Now, the use of the components q_i remove the degeneracy when $\theta=\pi/2$.

B. Dynamical evolution of Q

The dynamical equations for calamitic nematic liquid crystals can be determined by means of a variational principle originally put forward by Rayleigh [23]. For a conservative system, this principle asserts that the Rayleigh dissipation function evolves at a minimum rate, relatively to all its virtual values. This results in the balance of energy variations given by [24,25]

$$\delta\mathcal{D} + \delta\dot{\mathcal{F}} = 0, \tag{3}$$

where $\mathcal{D}$ is the Rayleigh dissipation function and $\dot{\mathcal{F}}$ is the rate of change of the free energy.

Neglecting the backflow effect, the dissipation density function D is expressed in the positive-definite quadratic form of a time derivative of **Q**,

$$\mathcal{D} = \int_V D dV = \int_V \gamma \,\mathrm{tr}\,\dot{\mathbf{Q}}^2 dV, \tag{4}$$

where V is a volume and γ is related to Leslie's rotational viscosity $\gamma_1=\gamma * S_{\mathrm{expt}}$, where S_{expt} is the experimental scalar order parameter [1].

The variation of the dissipation function can be determined from the expression (4) and its density is

$$\frac{\partial D}{\partial q_i}\delta q_i = 2\gamma\,\mathrm{tr}\left(\dot{\mathbf{Q}}\frac{\partial \mathbf{Q}}{\partial q_i}\right)\delta\dot{q}_i, \tag{5}$$

where $\dot{q}_i$ is the time derivative of q_i.

The relevant terms of the free energy $\mathcal{F}$ include $\mathcal{F}_d$, which is the elastic energy of the nematic texture distortion, $\mathcal{F}_t$, which is the thermotropic energy dictating the preferred material phase, $\mathcal{F}_e$, which is the electric energy due to an external electric field and $\mathcal{F}_s$, which is the surface energy, i.e., the nematic molecular interaction with the confining substrate.

$\mathcal{F}$ reads as

$$\mathcal{F} = \mathcal{F}_d + \mathcal{F}_t + \mathcal{F}_e + \mathcal{F}_s = \int_V (F_d + F_t + F_e)dV + \int_A F_s dA, \tag{6}$$

where F_d, F_t, F_e, and F_s are the corresponding energy densities and A is the boundary surface of the volume V. It is assumed that the thermotropic energy density $\mathcal{F}_t$ and the surface energy density $\mathcal{F}_s$ depend only on $\mathbf{Q}$,

$$F_t = F_t(\mathbf{Q}),$$

$$F_s = F_s(\mathbf{Q}),$$

whereas the elastic energy $\mathcal{F}_d$ and the electric energy $\mathcal{F}_e$ depend on $\mathbf{Q}$ and all of its first-order spatial derivatives, i.e.,

$$F_d = F_d(\mathbf{Q}, \nabla\mathbf{Q}),$$

$$F_e = F_e(\mathbf{Q}, \nabla\mathbf{Q}).$$

Higher order differentials of $\mathbf{Q}$ are neglected [1,22].

The rate of the change of the free energy density is

$$\delta\dot{\mathcal{F}} = \left[\frac{\partial F_b}{\partial q_i} - \frac{\partial}{\partial x_j}\left(\frac{\partial F_b}{\partial q_{i,j}}\right)\right]\delta q_i, \tag{7}$$

where $F_b = F_d + F_t + F_e$ is the bulk free energy density, "j" in the subscript denotes differentiation with respect to the spatial coordinate x_j, and summation over repeated indices is assumed. Since both the variations $\delta\dot{q}_i$ and the volume V are arbitrary, the Eqs. (3), (5), and (7) can be restated together,

$$\frac{\partial D}{\partial q_i} = \frac{\partial}{\partial x_j}\left(\frac{\partial F_d}{\partial q_{i,j}}\right) + \frac{\partial}{\partial x_j}\left(\frac{\partial F_e}{\partial q_{i,j}}\right) - \frac{\partial F_t}{\partial q_i} - \frac{\partial F_d}{\partial q_i} - \frac{\partial F_e}{\partial q_i}$$

$$(i = 1, \ldots, 5). \tag{8}$$

The solution of the system constituted by the five coupled partial differential equations (8) is univocally determined if suitable boundary conditions are imposed on the bounding substrates. In the following, each term of the free energy density and different boundary conditions are described in detail.

C. Free energy density

The thermotropic energy density F_t term is expressed as a Taylor expansion truncated at the fourth order around $\mathbf{Q}=0$ [1]. A fourth-order expansion is sufficient to have the isotropic and the nematic states as local minima of the free energy. It is worth to mention that a sixth-order expansion would be required in order to allow us a stable nematic biaxial state [26],

$$F_t = a\ \mathrm{tr}(\mathbf{Q}^2) - \frac{2b}{3}\mathrm{tr}(\mathbf{Q}^3) + \frac{c}{2}[\mathrm{tr}(\mathbf{Q}^2)]^2. \tag{9}$$

The coefficients a, b, and c are in general temperature dependent, although usually it is assumed $a = \alpha(T - T^*) = \alpha\Delta T$, where $\alpha > 0$ and T^* is the supercooling temperature, while b and c are assumed temperature independent [1]. For any nonpositive value ΔT, the equilibrium order parameter S_{eq} of a uniaxial nematic system is given by

$$S_{eq}(\Delta T) = \frac{b}{4c}\left(1 + \sqrt{1 - \frac{24ac}{b^2}}\right). \tag{10}$$

F_d is the free energy density term associated with any spatial gradient of $\mathbf{Q}$. The symmetry of our material does not allow all combinations of $\mathbf{Q}$ derivatives and the most general expression for F_d is [27]

$$F_d = \frac{L_1}{2}\left(\frac{\partial Q_{ij}}{\partial x_k}\right)^2 + \frac{L_2}{2}\frac{\partial Q_{ij}}{\partial x_j}\frac{\partial Q_{ik}}{\partial x_k} + \frac{L_6}{2}Q_{lk}\frac{\partial Q_{ij}}{\partial x_l}\frac{\partial Q_{ij}}{\partial x_k}, \tag{11}$$

where Q_{ij} is the (i,j) element of $\mathbf{Q}$ and the elastic parameters L_1, L_2, and L_6 are related to the Frank elastic constants k_{11}, k_{22}, and k_{33},

$$L_1 = \frac{1}{6S_{eq}^2}(k_{33} - k_{11} + 3k_{22}),$$

$$L_2 = \frac{1}{S_{eq}^2}(k_{11} - k_{22}),$$

$$L_6 = \frac{1}{2S_{\mathrm{expt}}^3}(k_{33} - k_{11}).$$

It can be demonstrated that there are seven elastic terms of cubic order [28] but only one, L_6, included in Eq. (11), ensures the correct mapping from the $\mathbf{Q}$ tensor to the Frank energy and it allows us to remove the $k_{11}=k_{33}$ degeneracy [29].

The presence of an irrotational electric field, $\boldsymbol{E} = -\nabla U$, gives rise to the electric energy density, which self-induces an internal electric field due to the dielectric and spontaneous polarization effects,

$$F_e = -\int \boldsymbol{D}d\boldsymbol{E}, \tag{12}$$

where $\boldsymbol{D}$ is the displacement field and $\boldsymbol{E}$ is the electric field. The constitutive equation which relates $\boldsymbol{D}$, $\boldsymbol{E}$, and the internal polarization $\boldsymbol{P}$ is

$$\boldsymbol{D} = \epsilon_0\boldsymbol{E} + \boldsymbol{P} = \epsilon_0\boldsymbol{E} + \boldsymbol{P}_i + \boldsymbol{P}_s = \epsilon_0\boldsymbol{E} + \epsilon_0\boldsymbol{\chi}\boldsymbol{E} + \boldsymbol{P}_s = \epsilon_0\boldsymbol{\epsilon}\boldsymbol{E} + \boldsymbol{P}_s, \tag{13}$$

where $\boldsymbol{P}_i$ and $\boldsymbol{P}_s$ are, respectively, the induced and the spontaneous polarizations. $\boldsymbol{P}_i$ depends on the dielectric susceptibility $\boldsymbol{\chi}$ and on $\boldsymbol{E}$. The quantity ϵ_0 is the vacuum electric permeability constant and $\boldsymbol{\epsilon}$ is the dielectric tensor, which describes the local anisotropy response of the nematic ordering to $\boldsymbol{E}$. One common expression of $\boldsymbol{\epsilon}$ [22] is

$$\boldsymbol{\epsilon} = \epsilon_a\mathbf{Q} + \epsilon_i\mathbf{I}, \tag{14}$$

where ϵ_a and ϵ_i are, respectively, the anisotropic and isotropic dielectric susceptibilities,

$$\epsilon_a = (\epsilon_\parallel - \epsilon_\perp)/S_{eq},$$

$$\epsilon_i = (\epsilon_\parallel + 2\epsilon_\perp)/3,$$

and $\epsilon_\parallel$ and $\epsilon_\perp$ are the parallel and perpendicular dielectric nematic constants.

The spontaneous polarization is assumed to derive only from flexoelectric effects. Therefore, $\boldsymbol{P}_s$ is written in terms of $\mathbf{Q}$ as [30]

$$\boldsymbol{P}_s = \bar{e}\,\nabla\,\mathbf{Q}, \tag{15}$$

where the ith component of $\boldsymbol{P}_s$ is

$$(P_s)_i = \bar{e}\frac{\partial Q_{ij}}{\partial x_j}$$

and $\bar{e}$ is the average flexoelectric coefficient, which is expressed as

$$\bar{e} = \frac{e_{11} + e_{33}}{2S_{eq}},$$

where e_{11} and e_{33} are the splay and bend flexoelectric coefficients of the nematics. Using Eqs. (12)–(15), the electric density energy F_e can be expressed as

$$\begin{aligned} F_e &= -\int (\epsilon_0 \boldsymbol{\epsilon} \boldsymbol{E} + \boldsymbol{P}_s) d\boldsymbol{E} \\ &= -\frac{\epsilon_0}{2}(\boldsymbol{\epsilon E}) \cdot \boldsymbol{E} - \boldsymbol{P}_s \cdot \boldsymbol{E} \\ &= -\frac{\epsilon_0}{2}(\epsilon_i |\nabla U|^2 + \epsilon_a \nabla U \cdot \mathbf{Q} \nabla U) + \bar{e}\,\nabla\,\mathbf{Q} \cdot \nabla U. \end{aligned} \tag{16}$$

The boundary conditions at the liquid crystal interfaces are taken into account by the surface term F_s. For rigid anchoring, this is equivalent to impose the Dirichlet condition on the surface,

$$\mathbf{Q} = \mathbf{Q_s}, \tag{17}$$

where $\mathbf{Q_s}$ is the prescribed order tensor promoted by the surface. In this case the boundary conditions are fixed and F_s does not play any role. For weak anchoring, we must take into account the interaction between the nematic molecules close to the substrate and the substrate itself. In this case the form of the interaction energy is given by

$$F_s = \frac{W_s}{2}\mathrm{tr}(\mathbf{Q} - \mathbf{Q_s})^2, \tag{18}$$

where W_s is the anchoring strength and $\mathbf{Q_s}$ is the value of the tensor order parameter preferred by the surface. Expression (18) is the generalization of the classical Rapini-Papoular anchoring energy using the tensor formalism [31]. The stable solution of $\mathbf{Q}$ must satisfy the system equations (8) and, on the boundary, the Neumann condition

$$\frac{\partial F_s}{\partial q_i} + \nu_j \frac{\partial F_b}{\partial q_{i,j}} = 0 \quad (i = 1, \ldots, 5), \tag{19}$$

where ν_j is the jth component of the outward vector normal to the substrate. This expression allows us to impose on the surface substrate uniaxial as well as biaxial conditions, since the nematic phase is described by $\mathbf{Q_s}$.

Moreover, the electric field $\boldsymbol{E}$ inside the cell must satisfy, in the static case with no free charges, the electrostatic Maxwell equations,

$$\nabla \cdot \boldsymbol{D} = 0, \tag{20}$$

$$\nabla \times \boldsymbol{E} = 0. \tag{21}$$

Equation (21) is automatically satisfied, because the electric field is conservative. Equation (20) is then the governing equation for the electric potential U,

$$0 = \nabla \cdot \boldsymbol{D} = \nabla \cdot (-\epsilon_0 \boldsymbol{\epsilon} \nabla U + \boldsymbol{P}_s) = 0. \tag{22}$$

Solving Eq. (22) is equivalent to minimizing the electric energy density (16) with respect to U. By making the electric potential U continuous through the cell, we ensure the standard conditions for the electrostatic: At material boundaries, the component of the electric field parallel to the interface is continuous and the normal component of the displacement field is also continuous. Typically boundary conditions for the potential U are

(i) fixed voltage on the electrodes;

(ii) spatial normal derivative of the potential equal to zero on the outer boundaries of the supporting substrate where no electrodes are present.

The first case corresponds to Dirichlet conditions, which are implemented forcing the potential value on the electrodes by matrix operations. Neumann conditions, corresponding to the second case, are naturally satisfied with the finite element method by assuming that the electric energy is totally confined in the liquid crystal material as well as in the substrate regions.

In addition to Dirichlet and Neumann conditions on $\mathbf{Q}$ and U, we have also used a periodic boundary condition on the lateral boundaries of the domain.

In the Appendix we describe the practical numerical procedures used to solve the resulting nonlinear system of partial differential equations.

III. BIAXIAL DOMAINS INSIDE A CALAMITIC PHASE

As previously mentioned, recent experiments on highly frustrated liquid crystal systems have shown that transient bulk biaxiality can be mechanically induced in calamitic nematic materials [10,11]. Moreover, the biaxial order reconstruction in nematics also allows fast electric coherent switching between two topologically inequivalent nematic textures inside a π cell [8,32]. In fact, up to now, the π cell is the main system used to experimentally investigate this phenomenon [12–14,33,34].

The π cell has sandwich geometry, with a thin film of nematic contained between two flat glass plates. The alignment on both surfaces induces a uniform pretilt angle θ with strong anchoring energy. The two plates are oriented to admit two topological different equilibrium nematic textures inside the cell: In the first one the nematic director is almost parallel to the surface plates with a slight splay distortion, without

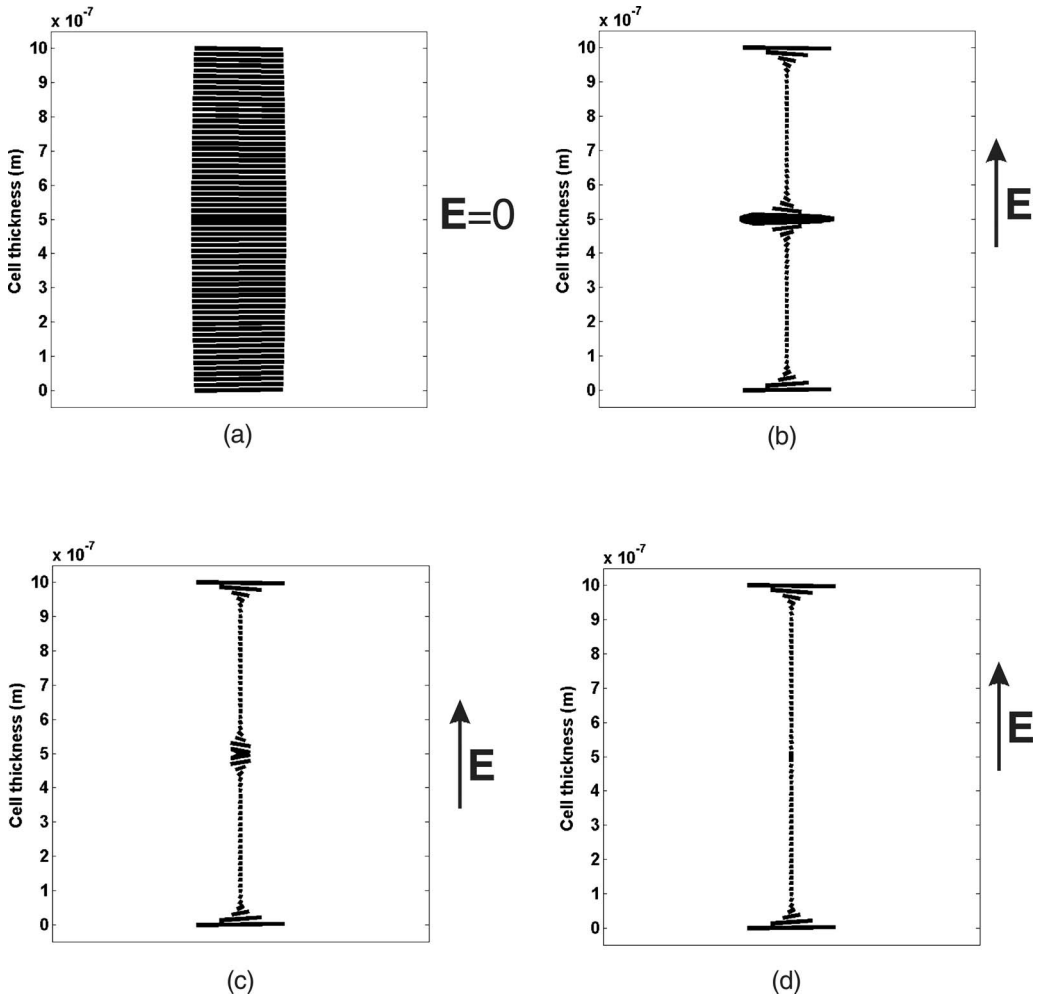

FIG. 1. One-dimensional representation of the nematic director configurations inside a 1-μm-thick π cell submitted to an external electric pulse with amplitude 11.4 V/μm at different times after the electric field is switched on: (a) $t=0$, (b) $t=60$ μs, (c) $t=70$ μs, (d) $t=90$ μs. The electric field is applied along the cell thickness.

any torsion; in the second one, the nematic director presents a mainly vertical alignment with a bend texture, which is topologically equivalent to a twisted configuration, i.e., with a torsion of π of the nematic texture itself. The splay and bend nematic textures of the π cell have distinct optical properties and they cannot be transformed one into another with simple director rotations. The connection is only possible by breaking somewhere the starting nematic texture and reconstructing it with or without the π torsion. This could be achieved, for instance, by melting the nematic order in a plane, but, in practice, the nematic biaxial order reconstruction is a mechanism which also enables an escape from topological constraints, requiring less energy than full melting.

To model this transient biaxial phenomenon, we discretize a 1-μm-thick one-dimensional π cell with quadratic finite elements with Dirichlet anchoring conditions on the boundary plates. The time-dependent **Q** configuration is the solution of the system composed by the five coupled Euler-Lagrange equations (8) and by the additional partial differential equation (22) for the electric potential U. The initial splay configuration has a tilt angle which varies almost linearly with z between $\theta_l=10°$ on the lower surface to $\theta_u=-10°$ on the upper surface, with θ measured with respect to the surface. A fast rectangular pulse electric field, strong enough to achieve the order reconstruction threshold, with amplitude $E=11.4$ V/μm is applied at the time $t=0$ s for a duration $t=100$ μs. The time step size for the calculation is $\delta t=0.1$ μs. The numerical simulation has been carried out by using typical calculation parameters for the nematic 5CB (4-cyano-4′-*n*-pentylbiphenyl) for $\Delta T=-2$ °C [35]. In this case one has the biaxial nematic coherence length $\xi_b=\sqrt{L/(S_{eq}b)}\approx 3$ nm. We have used a finer mesh in the center (the minimum element size is 0.1 nm) and coarser in the rest of the domain (with a maximum mesh size of 10 nm) since we expect that the biaxial region will arise in the middle of the cell.

Figure 1 shows, for different times, the distribution inside the cell of the director $\boldsymbol{n}$ (eigenvector of **Q** associated to its maximum eigenvalue). At $t=0$ s [Fig. 1(a)] the texture is slightly splayed and in the middle of the cell the director is parallel to the two flat boundary surfaces. The application of the electric field forces the nematic molecules to reorient in the vertical direction, perpendicularly to the boundary plates. At $t=60$ μs [Fig. 1(b)], the nematic molecules are every-

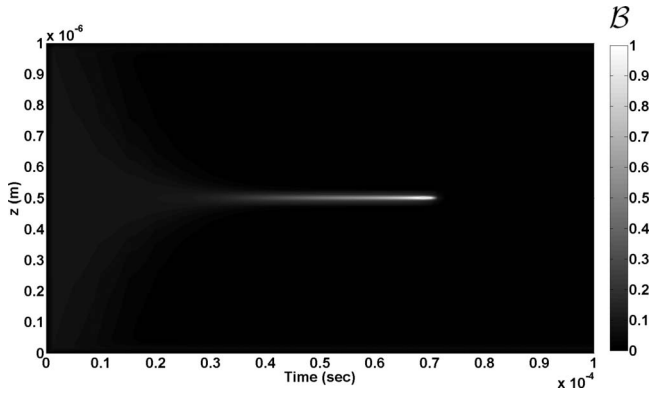

FIG. 2. One-dimensional dynamical representation of biaxiality inside a 1-μm-thick π cell submitted to an external electric pulse in the time interval $0 \leq t \leq 100$ μs. The white color is associated to the maximum value of the biaxiality, while the black color is associated to the uniaxial phase. The vertical axis represents the cell thickness, the time is represented along the horizontal axis. The electric field is applied along the cell thickness.

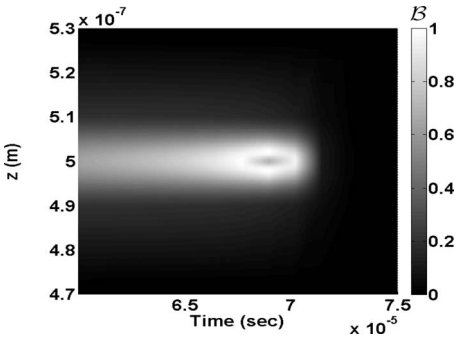

FIG. 3. Enlargement of Fig. 2 around $t=70$ μs, when the biaxial wall disappears. Note the volcano structure assumed during its dynamical evolution by the biaxial wall before it disappears. It is reminiscent of the core of a nematic defect, as shown in Fig. 4.

where parallel to the electric field except for three thin regions: One in the middle of the cell and two surface layers, where the nematic director keeps its initial quasiplanar orientation. The maximum distortion arises in the center of the cell: A biaxial region of thickness comparable with the biaxial coherence length ξ_b starts growing to connect the homeotropic upper and lower textures with the central planar orientation. At $t=70$ μs [Fig. 1(c)] the biaxial wall is destroyed and the initial splay texture is transformed into a bend one [Fig. 1(d)]. After the field is switched off ($t>100$ μs), the director begins a spontaneous viscoelastic relaxation.

In order to monitor the bulk order reconstruction, we use the invariant measure of the biaxiality given in [8],

$$\mathcal{B} = \sqrt{1 - \frac{6[\mathrm{tr}(\mathbf{Q}^3)]^2}{[\mathrm{tr}(\mathbf{Q}^2)]^3}}. \tag{23}$$

$\mathcal{B}$ varies between 0 and 1. In uniaxial states, $\mathcal{B}$ is zero. Its maximum value corresponds to the case of a biaxial phase in which one of the eigenvalues vanishes. The temporal evolution of the biaxiality $\mathcal{B}$ inside the π cell for the interval $0 \leq t \leq 100$ μs is shown in Fig. 2. The white color represents the maximum value of the biaxiality, while the black color corresponds to $\mathcal{B}=0$. All the other possible values of biaxiality are linearly mapped as gray levels between the white and the black colors.

$\mathcal{B}$ remains almost equal to 0.1 close to the boundaries where the strong anchoring prevents reorientation and it grows in the center of the cell where the biaxial wall is formed. At $t=70$ μs the nematic configuration in the center of the cell becomes purely biaxial with $\mathcal{B}=1$ and the transition to the bend texture shown in Fig. 1(c) takes place (see also Fig. 3, which is an enlargement of Fig. 2, around $t=70$ μs). The biaxial region surrounding the center has a size comparable with ξ_b and looks like a crater of a volcano, where $\mathcal{B}$ is zero inside and around the crater. The temporal evolution of the biaxial order induced by the electric field can be considered the dynamical equivalent of the spatial order evolution inside a defect [6]. In both cases, two distinct uniaxial orientations, perpendicular one to each other, are connected by intermediate biaxial states.

This analysis can be extended also when the nematic order reconstruction takes place close to a surface. The numerical calculation shows that, if the boundary conditions are not symmetric, the biaxial wall will not appear in the middle of the cell, but it could move toward one of the two boundary plates [36]. A very recent theoretical study has investigated the possibility to induce a surface order reconstruction on a hybrid cell by means of an external electric field [37]. In particular this approach has shown the influence of the electric field amplitude on the position and on the structure of a line defect of one-half charge, neglecting its dynamical behavior. Now we use the time-dependent $\mathbf{Q}$ tensor equations (8) in two-dimensional geometry to investigate how the core structure is influenced by the electric field of amplitude E_a and by the boundary surface as it moves inside the cell.

We now consider the 5CB at $\Delta T=-2$ °C confined between two parallel plates in a rectangular region whose thickness is $d_z=1$ μm and whose length is $d_x=4$ μm. The length d_x was chosen larger than the thickness d_z to avoid boundary effects on the defect line. Since $\nabla\mathbf{Q}$ is expected not to be homogeneous inside the cell, an adaptive mesh is employed which allows a finer discretization in the region of large $\nabla\mathbf{Q}$. In particular, the domain is discretized in triangular elements in which $\mathbf{Q}$ is approximated by quadratic Lagrange finite elements. As the biaxial coherence length is $\xi_b \approx 3$ nm, we use a mesh of maximum size of a few angstrom around the defect and a few nanometers in the rest of the domain. The boundary conditions used for the surface plates to align the nematic molecules are homeotropic on the upper plate and planar on the lower plate, with infinite anchoring energies on both plates. These boundary conditions are compatible with the germination of a line defect with topological charge $M=-1/2$. In the absence of an electric field, the defect is located in the middle of the cell, its position is stable and it is only determined by the boundary conditions. The maximum biaxiality is reached in the ring surrounding the core of the defect as shown in Fig. 4.

We also study the dynamics of the system in the presence of an electric field strong enough to modify the structure of the defect. We start at $t=0$ from the initial condition $\mathbf{Q}_{eq}$ and

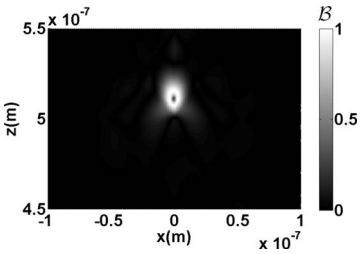

FIG. 4. Two-dimensional representation of biaxiality inside a vertical section of a hybrid cell of thickness 1 μm and width 4 μm in the absence of electric field. The homeotropic alignment is given by the upper boundary condition and the planar orientation by the lower boundary condition. The defect presents the usual volcano structure: The maximum biaxiality is around the core, while inside the core the nematic phase is uniaxial.

we apply a vertical electric field of amplitude $E_a = 14$ V/μm along the z axis for a time interval of $t_E = 150$ μs. The time step for the calculation is 0.1 μs. The electric field tends to enforce a homogeneous nematic alignment along the vertical axis. For $E < E_a$ the defect core does not vary its structure as it moves toward the bottom plate. For higher electric field, the defect exhibits a dramatic change in the core configuration as it interacts with the lower surface substrate.

Figures 5 and 6 show the biaxiality $\mathcal{B}$ around the defect core at different times in the presence of the electric field E_a. Nematic molecules that are farther from the line defect realign sooner than the nematic molecules that surround the defect, where it is concentrated the most on the elastic distortion. As a consequence, the line defect moves from its initial position and it is pushed toward the bottom plate. For $t > 10$ μs, although the defect distance from the lower plate is larger than the biaxial coherence length ξ_b, the defect core begins to lose its circular cross section and stretches along the z direction. The infinite energy anchoring on the lower surface influences the defect core structure: The nematic molecules that are located below the biaxial defect core tend to remain planar to the surface, opposing the electric torque realignment. A biaxial region grows to connect the planar surface nematic texture and the defect forming a structure that looks like a comet tail. At the same time, the two competing nematic alignments close to the lower plate tend to establish a biaxial layer of thickness $\sim 2\xi_b$. This behavior is stronger and stronger as the defect moves along the cell approaching the lower substrate, as shown in Figs. 5(b)–5(d). At the time $t = 40$ μs [Fig. 6(a)], the distance between the defect core and the lower surface becomes a few biaxial coherence lengths and the defect starts to grow parallel to the surface. Now, while the size of the defect core along the z direction remains almost unchanged, the core dimension in the x direction increases monotonically as the defect moves toward the bottom surface. The defect totally loses its cylindrical symmetry extending in the horizontal plane. The core structure and the surface biaxiality are mutually affected, as shown in Figs. 6(b)–6(d). For $t \geq 50$ μs the distance of the defect is comparable with the size of the biaxial ring surrounding the defect core (i.e., $\sim 4\xi_b$), here the defect merges into the anchoring layer and the surface biaxiality increases.

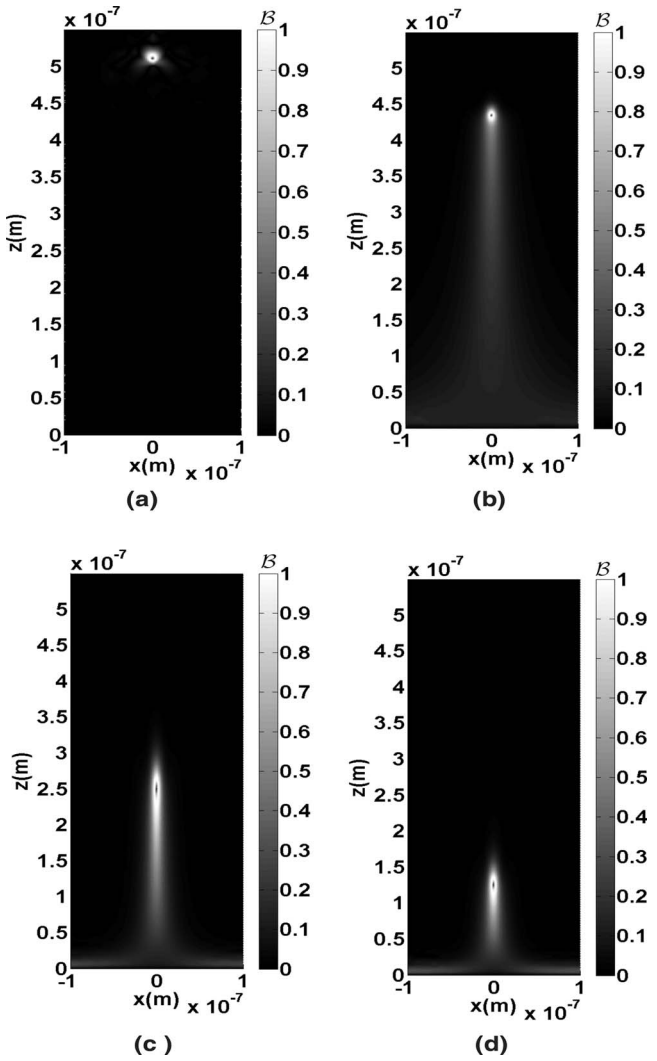

FIG. 5. Time sequence of the biaxiality around the defect for the electric amplitude $E_a = 14$ V/μm at $t = 0$ s (a), at $t = 20$ μs (b), at $t = 30$ μs (c), and at $t = 35$ μs (d). The electric field is applied along the z axis.

At $t = 150$ μs the defect core is completely stretched along the x direction forming, a continuous biaxial wall on the lower surface [Fig. 6(d)].

IV. CONCLUSION

A dynamical **Q** tensor model has been implemented using a finite element method. This numerical implementation is capable to handle arbitrary nematic liquid crystal confinement geometry whether one, two or eventually three dimensional. As examples we reported the dynamics of two calamitic systems, a π cell and a hybrid cell with a defect, both in the presence of an electric field. In both cases an applied electric field competes with the symmetry imposed to the system by the boundary conditions and a biaxial transient solution occurs to connect two competing nematic uniaxial textures. For the π cell, the electric field induces a bulk biaxial order reconstruction which destroys the nematic texture in one direction and reconstructs it in the orthogonal

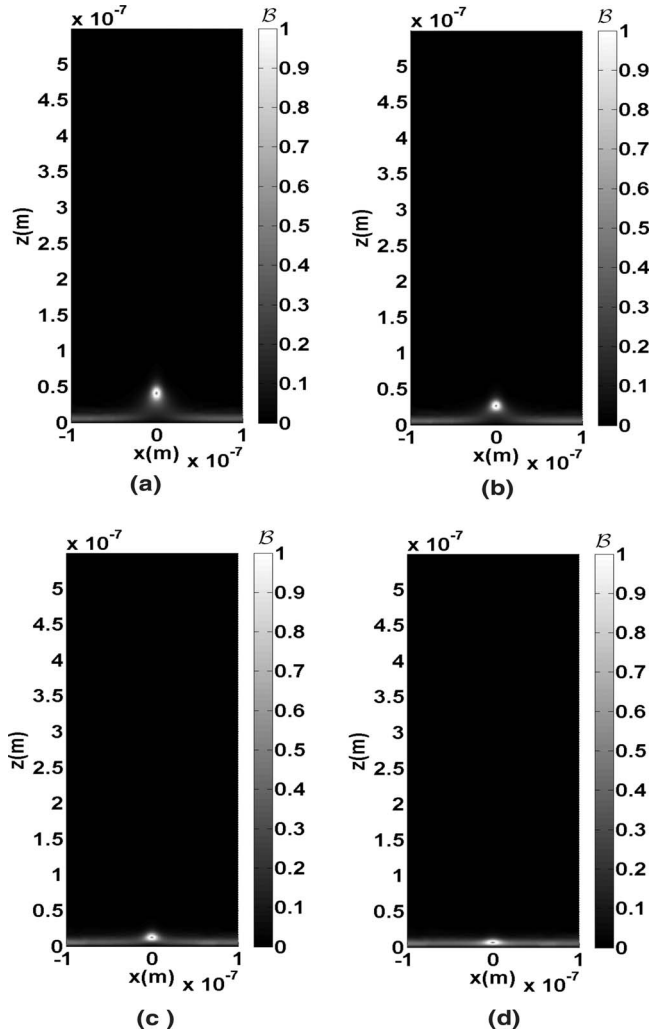

FIG. 6. Time sequence of the biaxiality around the defect for the electric amplitude $E_a=14$ V/μm at $t=42$ μs (a), at $t=45$ μs (b), at $t=50$ μs (c), and at $t=150$ μs (d). The electric field is applied along the z axis.

one. In the second case, asymmetric boundary conditions on the cell determine a stable line defect and, by applying a suitable electric field, a biaxial wall arises from the core defect. When the defect approaches the planar surface, the core stretches along the surface itself, increasing the biaxiality of the surface layer.

ACKNOWLEDGMENT

The authors acknowledge support from Italian National Research Council project LiCryL-MD.P10.009.

APPENDIX: MODEL OF THE Q TENSOR ORDER PARAMETER

Modeling the dynamics of the **Q** tensor inside a nematic cell in response to an external electric field generally starts off with minimizing the free energy within the cell. However, due to the high nonlinearity of the free energy expression coupled with electric effects, a direct solution of the **Q** deformation and the electric potential distribution is quasi-impossible. Therefore, the dynamical modeling usually involves an iteration process based on relaxation methods [21]: At each time step, the liquid crystal free energy is minimized to update the **Q** tensor profile and then this **Q** profile is used to solve Gauss law to update the potential profile. The initial distribution of **Q** can usually be preset by its boundary conditions. The stability of its iterative updating scheme is an important issue, which relies on a proper selection of updating time step Δt [38]. The solution for the above-mentioned iteration scheme includes two iterative steps:

(1) solving the **Q** distribution at a given potential profile;

(2) solving the potential distribution at a given **Q** profile.

A finite element method (FEM) is used to find the solution of the nonlinear partial differential system of equations.

1. Finite element method implementation

a. Q tensor update formulations via Galerkin's method

The high nonlinearity of Eq. (8) indicates that a direct solution is difficult to obtain. However, the Galerkin's method, a weighted residual method, associated to a weak formulation of the residual of the differential equations, can bypass this difficulty [15]. Suppose we divide the domain Ω into M element Ω^e with N nodes. In each element domain there are m nodes with m interpolation functions as well. In each element domain (e.g., eth element) the local **Q** tensor distribution can be interpolated by its m local node values using m local shape functions as

$$\tilde{\mathbf{q}}_i^e = \sum_{j=1}^{m} g_{ij}^e W_j^e \quad (i=1,\ldots,5), \tag{A1}$$

where g_{ij}^e and W_j^e are the jth node value and the interpolation function associated to the eth local element for the ith coefficient of the **Q** tensor matrix, respectively. The symbol $\tilde{\mathbf{q}}_i$ denotes an approximate solution of $\mathbf{q}_i$ which is usually different from the exact one. The form of the W_j^e is well defined and, for example, for a second-order shape function inside a triangle element is

$$W_j^e(x,y) = a_j^e + b_j^e x + c_j^e y + d_j^e x^2 + e_j^e x\cdot y + f_j^e y^2$$

$$(j=1,\ldots,m), \tag{A2}$$

the a_j^e, b_j^e, c_j^e, d_j^e, e_j^e, and f_j^e are coefficients that are determined by the node coordinate values and by the area of the triangle. Inserting $\tilde{\mathbf{q}}_i^e$ into Eq. (8) we can define the residual R_i^e, the error of the interpolation, in each element Ω^e,

$$R_i^e = \frac{\partial \tilde{D}^e}{\partial q_i} + \frac{1}{\gamma}[F_b]_{q_i}^e \quad (i=1,\ldots,5), \tag{A3}$$

where

$$[F_b]_{\tilde{q}_i}^e = \frac{\partial \tilde{F}_t}{\partial q_i} + \frac{\partial \tilde{F}_d}{\partial q_i} + \frac{\partial \tilde{F}_e}{\partial q_i} - \frac{\partial}{\partial x_j}\left(\frac{\partial \tilde{F}_d}{\partial q_{i,j}}\right) - \frac{\partial}{\partial x_j}\left(\frac{\partial \tilde{F}_e}{\partial q_{i,j}}\right).$$

The exact solution occurs only when R_i^e is equal to zero in each element. Due to the above approximation, the residual

R_i^e always leads to a nonzero value. However, with Galerkin's method, the residual R_i^e can be minimized in each element through weighting the residual R_i^e by the interpolation functions W_j^e that are the same shape functions used to interpolate $\mathbf{Q}$ as

$$\int_{\Omega_e} R_i^e W_j^e d\Omega^e = 0, \quad i = 1, \ldots, 5 \text{ and } j = 1, \ldots, m. \tag{A4}$$

Substituting $\tilde{\mathbf{q}}_i^e$ in the above equation and expanding it with a time difference scheme leads to

$$(q_i^e)^{t+\Delta t} = (q_i^e)^t + \Delta t[A^e]^{-1}(b^e), \quad i = 1, \ldots, 5, \tag{A5}$$

where $[\cdots]$ denotes a matrix and $(\cdots)$ denotes a vector, and for the ith element of the tensor order parameter $\mathbf{Q}$ one obtains that

$$A_{lm}^e = \int_{\Omega_e} W_l^e W_m^e d\Omega^e, \tag{A6}$$

$$b_m^e = -\int_{\Omega_e} \frac{1}{\gamma}[F_b]_{\tilde{q}_i}^e W_m^e d\Omega^e. \tag{A7}$$

As a result, the matrix A^e is symmetric, and its element values depend only on the geometry and the interpolation functions. A^e only needs to be calculated at the first iteration step and can be stored for the subsequent iteration steps. By applying the assembling process typical of a FEM procedure, the global matrix A and the global vector b can be obtained from the element matrix A^e and the element vector b^e [16].

b. Potential update formulations via Ritz's method

Once the $\mathbf{Q}$ tensor distribution is known inside the cell for the prescribed boundary conditions, the distribution of the electric potential inside the cell can be calculated by solving the Gauss law (22), or minimizing the electric energy system from a variational point of view. In our simulations we use the Ritz's method [15] to minimize the system electric energy, which inherits a more apparent physical and mathematical meaning than to apply the Galerkin's method in solving the Gaussian law. The electric energy $\mathcal{F}_e$ in the studied domain is equal to

$$\mathcal{F}_e = -\frac{1}{2}\int_{\Omega} \boldsymbol{D} \cdot \boldsymbol{E} d\Omega. \tag{A8}$$

Substituting $\boldsymbol{D}$ with the constitutive Eq. (13) and ensuring the conservative of electric field we restate (A8),

$$\mathcal{F}_e = \int_{\Omega} \frac{1}{2}\epsilon_0 \left(-\boldsymbol{\epsilon} \nabla U + \frac{2\boldsymbol{P}_s}{\epsilon_0} \right) \cdot \nabla U d\Omega. \tag{A9}$$

The approximate global potential solution $\tilde{U}$ can be expressed by the global node value U_k and global interpolation function W_k as

$$\tilde{U} = \sum_{k=1}^{N} U_k W_k. \tag{A10}$$

Thus, $\mathcal{F}_e$ is a function of N global variables $U_k (k = 1, 2, \ldots, N)$. To find an equilibrium solution for U, it is necessary to find a minimum of $\mathcal{F}_e$. This leads to N equations as

$$\frac{\partial \mathcal{F}_e}{\partial U_k} = 0, \quad k = 1, \ldots, N. \tag{A11}$$

This equation system can be further expressed as a matrix representation

$$[B](\tilde{U}) = (p), \tag{A12}$$

where, again $[\cdots]$ denotes a matrix and $(\cdots)$ denotes a vector. The matrix B is symmetric because the tensor dielectric $\boldsymbol{\epsilon}$ is a symmetric matrix. In particular the elements of B and p are, respectively,

$$B_{kh} = \epsilon_0 \int_{\Omega} \left(\frac{\partial W_k}{\partial x_1}, \frac{\partial W_k}{\partial x_2}, \frac{\partial W_k}{\partial x_3} \right) \cdot \left[\boldsymbol{\epsilon} \left(\frac{\partial W_h}{\partial x_1}, \frac{\partial W_h}{\partial x_2}, \frac{\partial W_h}{\partial x_3} \right)^T \right] d\Omega, \tag{A13}$$

$$p_k = \int_{\Omega} \frac{2\boldsymbol{P}_s}{\epsilon_0} \cdot \left(\frac{\partial W_k}{\partial x_1}, \frac{\partial W_k}{\partial x_2}, \frac{\partial W_k}{\partial x_3} \right)^T d\Omega. \tag{A14}$$

[1] P. G. de Gennes and J. Prost, *The Physics Liquid Crystals* (Clarendon, Oxford, 1993).
[2] C. W. Oseen, Trans. Faraday Soc. **29**, 883 (1933).
[3] H. Zocher, Trans. Faraday Soc. **29**, 945 (1933).
[4] F. Frank, Discuss. Faraday Soc. **25**, 19 (1958).
[5] P. de Gennes, Phys. Lett. **30A**, 454 (1969).
[6] N. Schopohl and T. J. Sluckin, Phys. Rev. Lett. **59**, 2582 (1987).
[7] P. Palffy-Muhoray, E. Gartland, and J. Kelly, Liq. Cryst. **16**, 713 (1994).
[8] R. Barberi, F. Ciuchi, G. Durand, M. Iovane, D. Sikharulidze, A. Sonnet, and E. Virga, Eur. Phys. J. E **13**, 61 (2004).
[9] F. Bisi, E. C. Gartland, R. Rosso, and E. G. Virga, Phys. Rev. E **68**, 021707 (2003).
[10] G. Carbone, G. Lombardo, and R. Barberi (unpublished).
[11] B. Zappone, P. Richetti, R. Barberi, R. Bartolino, and H. T. Nguyen, Phys. Rev. E **71**, 041703 (2005).
[12] R. Barberi, F. Ciuchi, G. Lombardo, R. Bartolino, and G. E. Durand, Phys. Rev. Lett. **93**, 137801 (2004).
[13] F. Ciuchi, H. Ayeb, G. Lombardo, R. Barberi, and G. Durand, Appl. Phys. Lett. **91**, 244104 (2007).
[14] H. Ayeb, F. Ciuchi, G. Lombardo, and R. Barberi, Mol. Cryst. Liq. Cryst. **481**, 73 (2008).
[15] O. Zienkiewicz and R. Taylor, *The Finite Element Method*

(Butterworth-Heinemann, Oxford, 2002), Vol. I.
[16] Y. Known and H. Bang, *The Finite Element Method Using Matlab* (CRC Press, Boca Raton, FL, 2000).
[17] L. Moreau, P. Richetti, and P. Barois, Phys. Rev. Lett. **73**, 3556 (1994).
[18] K. Kočevar, A. Borštnik, I. Muševič, and S. Žumer, Phys. Rev. Lett. **86**, 5914 (2001).
[19] G. Carbone, R. Barberi, I. Musevic, and U. Krzic, Phys. Rev. E **71**, 051704 (2005).
[20] L. V. Mirantsev and E. G. Virga, Phys. Rev. E **76**, 021703 (2007).
[21] J. Anderson, P. Watson, and P. Bos, *LC3D: Liquid Crystal Display 3-D Directory Simulator, Software and Technology Guide* (Artech House, Boston, 1999).
[22] E. Virga, *Variational Theories for Liquid Crystals* (Chapman-Hall, London, 1994).
[23] J. Strutt, Proc. London Math. Soc. **s1-4**, 357 (1871).
[24] A. M. Sonnet and E. G. Virga, Phys. Rev. E **64**, 031705 (2001).
[25] A. Sonnet, P. Maffettone, and E. Virga, J. Non-Newtonian Fluid Mech. **119**, 51 (2004).
[26] E. Gramsbergen, L. Longa, and W. de Jeu, Phys. Rep. **135**, 195 (1986).
[27] H. Mori, E. Gartland, J. Kelly, and P. Bos, Jpn. J. Appl. Phys., Part 1 **38**, 135 (1999).
[28] K. Schiele and S. Trimper, Phys. Status Solidi B **118**, 267 (1983).
[29] D. W. Berreman and S. Meiboom, Phys. Rev. A **30**, 1955 (1984).
[30] A. Alexe-Ionescu, Phys. Lett. A **180**, 456 (1993).
[31] M. Nobili and G. Durand, Phys. Rev. A **46**, R6174 (1992).
[32] P. Martinot-Lagarde, H. Dreyfus-Lambez, and I. Dozov, Phys. Rev. E **67**, 051710 (2003).
[33] S. Joly, I. Dozov, and P. Martinot-Lagarde, Phys. Rev. Lett. **96**, 019801 (2006).
[34] R. Barberi, F. Ciuchi, H. Ayeb, G. Lombardo, R. Bartolino, and G. E. Durand, Phys. Rev. Lett. **96**, 019802 (2006).
[35] B. Ratna and R. Shashidhar, Mol. Cryst. Liq. Cryst. **42**, 113 (1977).
[36] G. Lombardo, H. Ayeb, F. Ciuchi, M. P. DeSanto, R. Barberi, R. Bartolino, E. G. Virga, and G. E. Durand, Phys. Rev. E **77**, 020702(R) (2008).
[37] M. Ambrozic, S. Kralj, and E. G. Virga, Phys. Rev. E **75**, 031708 (2007).
[38] J. E. Anderson, C. Titus, P. Watson, and P. J. Bos, SID Int. Symp. Digest Tech. Papers **31**, 906 (2000).